Crystal-plane-dependent metal oxide-support interaction in CeO_2/g-C_3N_4 for photocatalytic hydrogen evolution

Weixin Zou[a,b,c], Biao Deng[b,c], Xixi Hu[b,c], Yipeng Zhou[b,c], Yu Pu[b,c], Shuohan Yu[c], Kaili Ma[b,c], Jingfang Sun[b,c], Haiqin Wan[a,c,*], Lin Dong[a,c]

[a] State Key Laboratory of Pollution Control and Resource Reuse, School of the Environment, Nanjing University, Nanjing 210093, PR China
[b] Key Laboratory of Mesoscopic Chemistry of MOE, School of Chemistry and Chemical Engineering, Nanjing University, Nanjing 210093, PR China
[c] Jiangsu Key Laboratory of Vehicle Emissions Control, Center of Modern Analysis, Nanjing University, Nanjing 210093, PR China

ABSTRACT

CeO_2 and its derivatives are potential photocatalysts due to their superior redox ability, abundant oxygen defects and cost effectiveness. However, little attention has been paid to the crystal-plane-dependent interactions in CeO_2-based nanocomposites for photocatalytic hydrogen evolution. In this work, CeO_2/g-C_3N_4 were synthesized with tunable CeO_2 crystal planes ({110}, {100}, and {111}). Photoelectrochemical, XPS, Raman, ESR results suggested that the electron-separation efficiency, oxygen defects and Ce^{3+}/Ce^{4+} reversibility pairs were greatly dependent on the crystal-faceted CeO_2 and g-C_3N_4 interaction, and the photocatalytic performances of hydrogen evolution under visible light irradiation were in the order: $CeO_2\{110\}/g$-C_3N_4 > $CeO_2\{100\}/g$-C_3N_4 > $CeO_2\{111\}/g$-C_3N_4 > g-C_3N_4. Furthermore, the FT-IR, XPS and density functional theory (DFT) calculations shown that the different properties of CeO_2/g-C_3N_4 were resulted from the built-in electric field at the interface, and more intensive electronic interaction was found on $CeO_2\{110\}/g$-C_3N_4, leading to the efficient separation and transfer of photo-generated electrons under light illumination.

1. Introduction

With the increasing populations and development, the search for sustainable energy is one of the most important issues [1]. Among the various renewable energy, the photocatalytic water splitting for H_2 production is considered as an effective way to utilize solar energy and solve the global energy problem [2,3]. Generally, most of solar radiation is in the form of visible light, and thus it is crucial and essential to explore photocatalysts with available visible light adsorption and highly efficient activity [4,5].

The most abundant rare metal oxide ceria (CeO_2), with the unique 4f electron structure, has attracted numerous attention in the field such as vehicle exhaust purification [6], water-gas shift reaction [7], oxygen sensors [8], and so on. Especially, CeO_2 has shown its advantages in photocatalytic water splitting [9], pollutant degradation [10], organic synthesis [11], due to its rich oxygen defects, superior redox ability and Ce^{3+}/Ce^{4+} electronic pair [12,13]. The fast recombination of electron-hole acts as a crucial problem for CeO_2 photocatalysts [14]. To mitigate the above challenge, several strategies have been exploited such as doping with non-metal or metal ions [4,15], anchoring metal

nanoparticles as co-catalysts [16], combining with semiconductor and carbonaceous materials [17,18]. The heterojunction of CeO_2 and visible active photocatalysts is an effective one, and with the help of the structure, photo-generated electrons and holes could be parted by the electric filed [19,20]. However, the performance on electron-hole separation of the CeO_2-based heterojunctions still need to be improved. Given the limited reserves and high cost of noble metals, it is of great significance to design the non-precious metal photocatalysts for H_2 evolution by CeO_2.

Graphitic carbon nitride (g-C_3N_4) is a promising two-dimensional non-metal material for photocatalysis, due to its excellent chemical and thermal stability, high nitrogen content, attractive electronic structure, and environment friendliness [21]. It has been reported that g-C_3N_4 could act as a flexible support to encapsulate CeO_2 nanocrystals by type II structure in many photocatalytic fields [20,22–24]. The g-C_3N_4/CeO_2-TiO_2 nanocompound was prepared for toluene removal by Muñoz-Batista et al., and the obtained nanocompound had better photocatalytic performance compared to the binary nanocompounds (C_3N_4/TiO_2, CeO_2-TiO_2) [20]. Li et al. designed mesostructured CeO_2/g-C_3N_4 for photocatalytic CO_2 reduction, and found that the

---

heterogeneous nanocomposites had greatly enhanced response to solar light, charge carrier separation and transfer [22]. Although photocatalytic performances of CeO_2/g-C_3N_4 have been studied, some fundamental questions still need to answer. As we known, various CeO_2 nanostructures with different crystal planes exhibit different properties such as redox ability, electronic structure and reactant molecule adsorption [25–27]. Through theoretical calculation, the oxygen vacancy formation energy of CeO_2 was in the order of {111} > {100} > {110} [25]. Li et al. proposed that the photo-generated electrons preferred on CeO_2 {111} plane, while holes encouraged to migrate to {100} plane [26]. Wu et al. found that the CO_2 adsorption was dependent on CeO_2 planes: {110} > {100} > {111} [27]. Based on that, CeO_2 nanoparticles with different crystal planes would have various interactions with the g-C_3N_4 support on the interfaces, resulting in different electronic structures and electron-hole separation abilities. In previous literatures, little attention was focused on the crystal-plane dependent metal oxide-support interaction in CeO_2/g-C_3N_4 for photocatalysis.

In this work, CeO_2 nanocrystals with {110}, {100}, and {111} planes exposed were anchored on g-C_3N_4 to investigate the metal oxide-support interaction. Dependent on the interfacial effect, CeO_2 {110}/g-C_3N_4 had more oxygen defects, faster photogenerated electron-hole separation and better photocatalytic H_2 evolution under visible light. Furthermore, XPS, FT-IR and DFT calculations are employed to reveal the interfacial charge interaction between CeO_2 crystals and g-C_3N_4 support, and the schematic illustration of interfaces was proposed. This study shown that engineering the crystal-plane-dependent metal oxide-support interaction could provide a scientific basis for the design of efficient photo-catalysts.

2. Experimental

2.1. Catalyst preparation

CeO_2/g-C_3N_4 composites with different crystal planes ({110}, {100}, {111}) were prepared *via* a two-step self-assembly, according to the literature [28]. The g-C_3N_4 support was obtained through the urea calcination in air at 550 °C for 4 h, afterward, the g-C_3N_4 was grounded and added to methanol under ultrasonic treatment for 0.5 h. Subsequently, CeO_2 rod {110}, cube {100}, octahedron {111} were prepared by the report [29], and dispersed in 50 mL methanol, respectively. Finally, the mixture of CeO_2 and g-C_3N_4 were ultrasonic for 0.5 h and stirred in a fume hood for 24 h to remove methanol. The obtained three solids were calcined in a muffle furnace at 150 °C for 4 h. The nominal weight ratio of CeO_2 to g-C_3N_4 was 5 wt%. The obtained samples CeO_2/g-C_3N_4 composites with different crystal planes ({110}, {100}, {111}) were denoted as rCN{110}, cCN{100}, oCN{111}, respectively. The g-C_3N_4 was denoted as CN.

2.2. Catalyst characterization

Transmission electron microscopy (TEM) characterization was taken on JEM-2100 instrument by an acceleration voltage of 200 kV. The sample was crushed and dispersed in ethanol, and the obtained suspension was dropped and dried on copper grids with carbon film. The crystal structures of rCN, cCN, oCN and CN were determined by X-ray diffraction (XRD) on Philips X'Pert Pro diffractometer under Ni-filtered Cu Kα radiation (λ = 0.15418 nm). The Brunauer–Emmet–Teller (BET) surface area was determined by nitrogen adsorption at 77 K on Micrometrics ASAP-2020 adsorption apparatus. The X-ray tube was operated at 40 kV and 40 mA. X-ray photoelectron spectroscopy (XPS) analysis was determined by PHI 5000 VersaProbe high performance electron spectrometer, on monochromatic Al Kα radiation (1486.6 eV), the sample was outgassed at room temperature in a UHV chamber (< 5×10^{-7} Pa). The charging effect on sample was compensated by binding energies referenced to 284.6 eV of C 1s peak. This reference provided binding energies with an error

within ± 0.1 eV. The FT-IR spectra were collected from 400 to 4000 cm^{-1} on Nicolet 5700 FT-IR spectrometer at the spectral resolution of 4 cm^{-1}. UV–vis diffuse reflectance spectroscopy (UV–vis DRS) was recorded in the range of 200–700 nm with the reference of $BaSO_4$ by a Shimadzu UV-2401 spectrophotometer. The electron spin resonance (ESR) signal was examined at 77 K on ESR JES FA200 (JEOL) spectrometer.

Electrochemical measurements on a CHI660E electrochemical workstation were measured *via* a standard three-electrode cell. The photocatalyst was deposited on fluorine-doped Tin Oxide used as a working electrode, while the reference and counter electrodes were Hg/Hg_2Cl_2 and platinum wire (in saturated KCl) electrodes, respectively. The 0.1 M Na_2SO_4 was electrolyte solution. A Xe lamp was employed as irradiation. Raman spectra were obtained on a LABRAM-HR Confocal Laser with He–Cd lasers (325 nm) excitation source.

2.3. Catalytic performances measurement

The photocatalytic hydrogen evolution reaction under visible light was carried out under 300 W Xe lamp irradiation with the 420 nm cut-off filter in a top-irradiation vessel connected to a gas-closed glass system. 50 mg sample was dispersed in 100 mL solution (10 mL triethanolamine and 90 mL deionized water). The H_2PtCl_6 aqueous solution was added and during the reaction Pt nanopaticles were in-situ reduced (3 wt% Pt). The temperature of reaction solution was kept around 6 °C by the circulation pump. The system was sealed and evacuated for 30 min before illumination and the generated hydrogen was measured by a gas chromatograph. The recycle experiment was performed as followed: every cycle was carried out for 5 h. During the interruption of each cycle, 10 mL triethanolamine was added into the reaction and the system was vacuumed for 30 min.

2.4. Computational details

All the theoretical computations were performed by using the Vienna Ab initio Simulation Package (VASP) based on plane-wave density functional theory (DFT) method [30–32]. The interaction between the ionic cores and electrons was described using the projector-augmented wave (PAW) method [33], and the Kohn-Sham valence electronic wavefunction was expanded in a plane-wave basis set with a kinetic energy cut-off of 400 eV. The exchange-correlation effects were represented by using the Perdew-Burke-Ernzerhof (PBE) functional of the generalized gradient approximation (GGA) [34]. To eliminate the error from strong self-interaction of localized Ce 4f-orbital, DFT + U method with the Ueff = 5.0 eV was used in all calculations [35,36]. Brillouin-zone integrations were performed using Monkhorst-Pack grids of special points [37] with $3 \times 3 \times 1$ meshes for the slab calculations of structural and electronic properties. The structural optimization was considered converged if the forces acting on the atoms were less than 0.05 eV/Å and the criteria of energy convergence was set to 1×10^{-4} eV. And spin polarization was taken into account in all calculations.

The optimized lattice parameters a = b = c = 5.466 Å for unit cell of CeO_2 and a = b = 7.089 Å for monolayer g-C_3N_4 were in good agreement with the experiments (a = b = c = 5.411 Å; a = b = 7.130 Å for g-C_3N_4) [38,39]. During constructing g-C_3N_4/CeO_2 heterostructures, we chose different shapes of periodic units for g-C_3N_4 to match the three crystallographic planes of CeO_2, which could be seen in Fig. S1 (in Supporting information). And (2×2) periodically repeated slab with five layers, (3×2) with nine layers and (2×2) with twelve layers were constructed to represent the models of CeO_2 (110), (100) and (111) surfaces, of which the number of fixed bottom layers was two, four and six, respectively. The vacuum space in the Z direction was around 20 Å, which was enough to separate the interaction between periodic images. The lattice mismatches caused by such constructions were shown in Table S1.
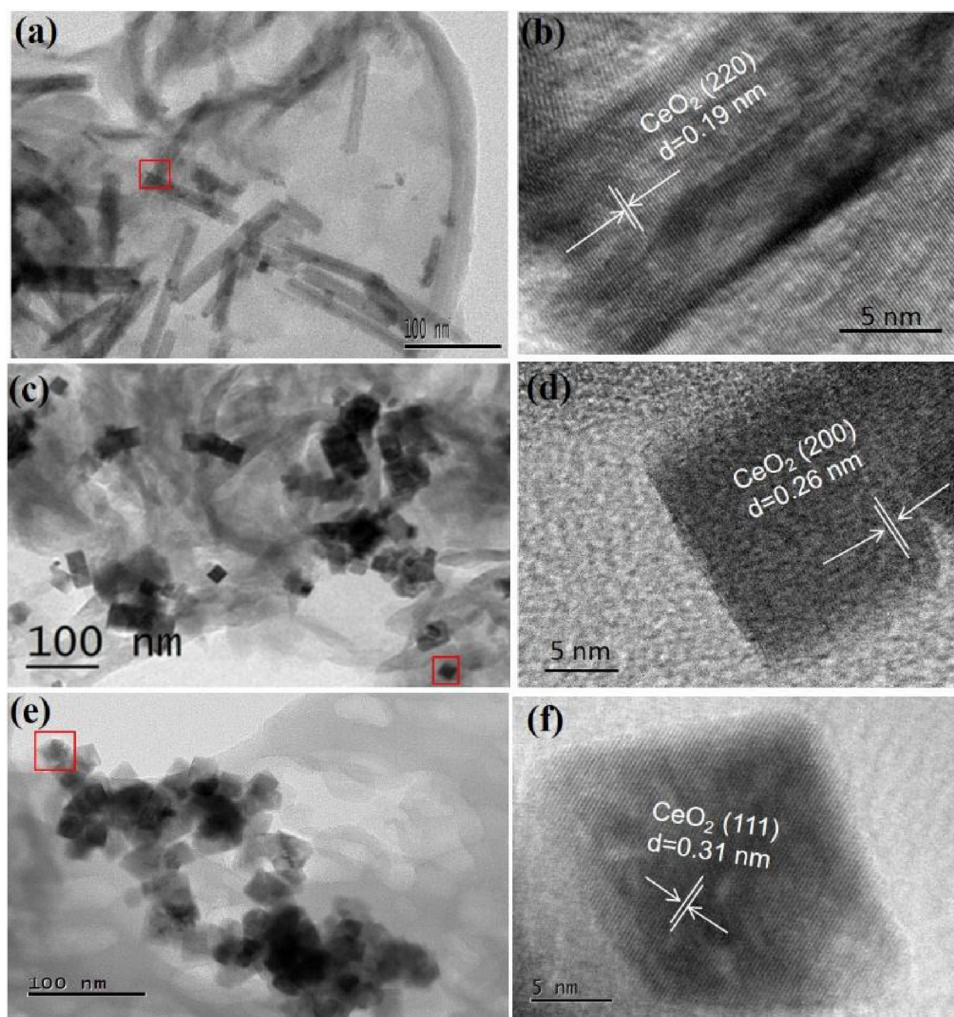
Fig. 1. TEM and HRTEM images of (a, b) rCN; (c, d) cCN; and (e, f) oCN (HRTEM image was the enlarged area of the red framed area in TEM image) (For interpretation of the references to colour in this figure legend, the reader is referred to the web version of this article.).

3. Results and discussion

3.1. Morphologies and structures

The TEM and high resolution (HR) TEM characterizations of CeO_2 nanocrystals with different morphologies (rods, cubes and octahedrons) were carried out, and the results were shown in Fig. S2. It was observed that the particles had the uniform shapes, the CeO_2 rods had the diameter of *ca.* 10 nm and the length of *ca.* 70 nm, and the average size of cubes and octahedrons were 30 nm. The HRTEM results suggested that the CeO_2 rods, cubes and octahedron were dominantly exposed {110}, {100} and {111} facets, respectively. Furthermore, the morphologies of the as-prepared CeO_2/g-C_3N_4 nanocomposites were shown. From Fig. 1a, c, e, well-defined CeO_2 nanocrystals (rods, cubes, and octahedron) were anchored on g-C_3N_4 support and CeO_2 rods had a better dispersion than others, which implied that stronger binding interactions might be present between CeO_2 rods and g-C_3N_4. According to the HRTEM images (Fig. 1b, d, f), the crystal lattices were 0.19, 0.27, 0.31 nm, which corresponded to {110}, {100}, {111} crystal planes, suggesting that the dominant crystal planes of CeO_2 rods, cubes, and octahedron were {110}, {100}, {111} planes, respectively.

The phase structures of as-prepared CeO_2/g-C_3N_4 (rCN{110}, cCN {100}, oCN{111}) nanocomposites and g-C_3N_4 (CN) were determined by XRD characterization. From Fig. S3, all samples displayed the diffraction peak at 27.3°, which were perfectly indexed as the CN (002)

plane and ascribed to the interlayer stacking [40]. In addition, the diffraction peaks of CeO_2 at *ca.* 28.5°, 33.1°, 47.4° were observed and ascribed to (111), (200), and (220) crystal planes, respectively (JCPDS no: 04-0802). In comparison with three CeO_2/g-C_3N_4 nanocomposites, the XRD patterns of CeO_2 on rCN were weaker than that on cCN, oCN samples, suggesting that the synergistic effect on rCN interface was stronger, leading to a better dispersion of CeO_2 rods on g-C_3N_4.

The surface areas of the as-synthesized CeO_2 nanocrystals and CeO_2/g-C_3N_4 composites were determined and the related results were displayed in Table S2. It was found that the surface areas of the as-synthesized CeO_2 nanocrystals were in the order of octahedron > rod > cube, and the introduce of CN was beneficial for the increased surface areas of the CeO_2/g-C_3N_4 composites, in the sequence of rCN > cCN > oCN, indicating that CeO_2 nanorods have a better dispersion than the two others on g-C_3N_4 composites, and then the interaction area between CeO_2 rods {110} and g-C_3N_4 was higher.

3.2. Oxygen defects

As we all known, the oxygen defects were important in many aspects [41–44], especially, the oxygen vacancy was beneficial for the photocatalytic H_2 evolution. For example, the reactant of water molecules were more inclined to be adsorbed on oxygen vacancy, and then the accessible surface was helpful for reducing the energy barrier in photocatalytic water splitting; in addition, the oxygen vacancy on
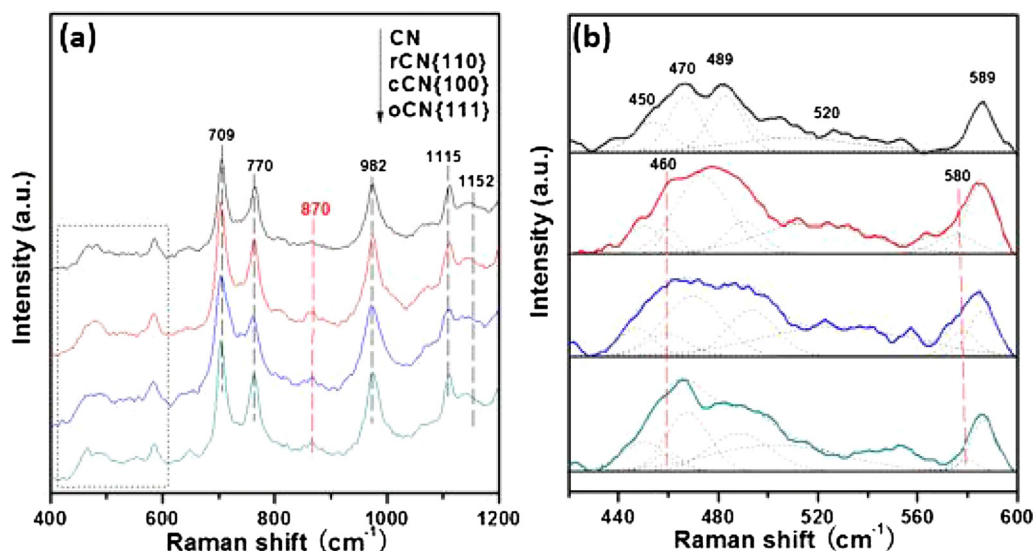
Fig. 2. (a) UV Raman spectra of CN, rCN, cCN, and oCN; (b) the enlarged Raman spectra from 410-600 cm^{-1}.

surface could decrease the recombination rate of photo-generated electrons and holes [45,46]. Therefore, we employed Raman, ESR and XPS to investigate the oxygen defect property of rCN{110}, cCN{100}, and oCN{111} in comparison. The Raman spectra of CN and CeO$_2$/g-C$_3$N$_4$ composites were shown in Fig. 2a. There was a broad band (410–600 nm), which was fitted by several peaks. The peaks at 450, 470, 520, 589, 709, 770, 982 cm^{-1} were derived from vibration (breathing modes of triazine ring, bending mode of graphitic domains) of CN [47–49]. In addition, the obtained three peaks at 460, 580, and 870 cm^{-1} were ascribed to the symmetric stretching vibrations mode F$_{2g}$ (O$_L$), oxygen defect (O$_v$), and peroxide species (O$^-$) adsorbed on defect sites of CeO$_2$, respectively [50,51]. In comparison with the Raman spectra of CeO$_2$ (Fig. S4), it was found that the couple with g-C$_3$N$_4$ made the CeO$_2$ peaks broad and the intensity of oxygen defect was enhanced. The relative concentration of oxygen defects (O$_v$, O$^-$) was calculated by the ratio of A$_{580+870}$/A$_{460}$ in CeO$_2$/g-C$_3$N$_4$ composites, and the order was rCN{110} > cCN{100} > oCN{111}. The above sequence suggested that oxygen defects formation was relied on the metal oxide-support interaction and more defects would be facilitated to generate on rCN than that on cCN and oCN. Furthermore, the XPS spectra of O 1 s on rCN, cCN and oCN were shown in Fig. 3a. The peaks

at 529.0, 530.0, and 531.5 eV were assigned to CeO$_2$ lattice oxygen (O$_L$), oxygen defects (O$_V$), and chemisorbed oxygen species on surface (O$_C$), respectively [52]. On the basis of that, there was more obvious signal of oxygen defects was observed rCN{110}.

Generally, the Ce^{3+} species and oxygen defects would generate simultaneously, owing to a charge compensation mechanism (Ce^{4+} + O$_L$→Ce^{3+} + O$_v$) [53]. In other words, the Ce^{3+} concentration could give useful information regarding of surface defects, which played a crucial role in enhancing the interfacial interaction and improved photocatalytic performance of ceria based systems. In addition, the generated Ce^{3+}/Ce^{4+} electronic pair was reversible, which was beneficial for charge transfer process in photocatalysis. Therefore, ESR characterization was used to measure the surface Ce^{3+} content, and the corresponding result was displayed in Fig. 3b. The ESR signal of g = 1.956 was recognized as Ce^{3+} species [54], and the signal intensity was stronger on rCN{110} than that on cCN{100} and oCN{111}, which suggested that more Ce^{3+} species was formed on the rCN sample. Moreover, the Ce 3d XPS spectra was measured in Fig. S5 to compare the relative ratio of Ce^{3+}/Ce^{4+} on rCN, cCN and oCN. The Ce 3d XPS peak was fitted into eight peaks. The content ratio of Ce^{3+} to Ce^{4+} was calculated by A$_{(u'+v')}$/A$_{(u'''+u''+u+v'''+v''+v)}$ [55], and found that the
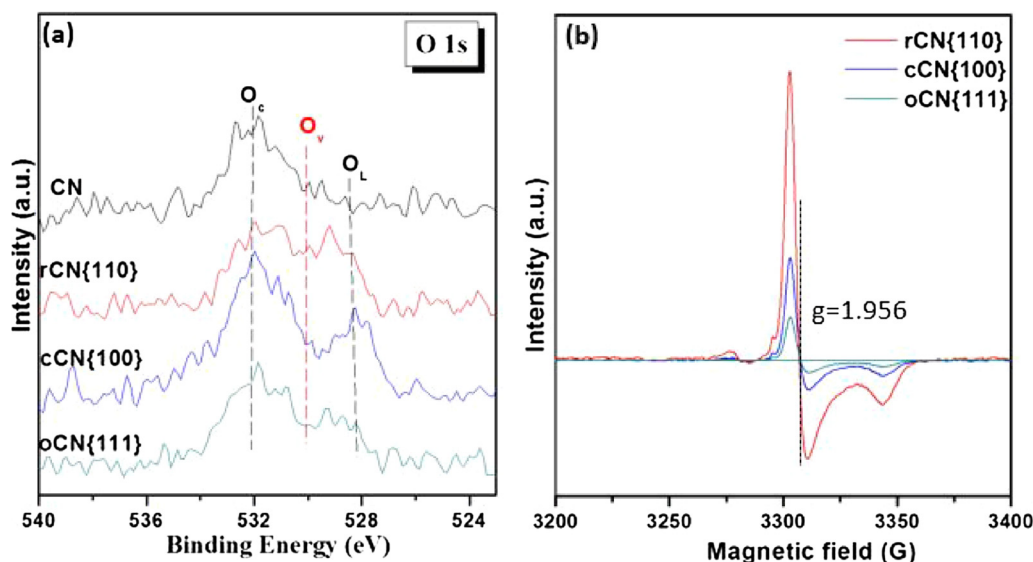

Fig. 3. (a) O 1 s XPS spectra of CN, rCN, cCN, and oCN; (b) ESR result of rCN, cCN, and oCN.

Ce^{3+} content in rCN was higher than that of cCN and oCN, consistent with ESR result. On the basis of the above Raman, ESR and XPS characterizations, rCN{110} had the highest oxygen defects and the ration of Ce^{3+}/Ce^{4+}, cCN{100} was followed, and oCN{111} was lowest.

3.3. Optical and photoelectrochemical properties

To identify the optical properties of the various $CeO_2/g-C_3N_4$ composites, the UV–vis DRS was characterized and the corresponding results were shown in Fig. S6. The CN sample exhibited a strong absorption edge at *ca.* 450 nm. After hybridization of $g-C_3N_4$ with CeO_2, it was observed that the absorption edge was red-shifted compared with bare $g-C_3N_4$, resulted in more available visible light adsorption. In addition, the UV–vis DRS and the corresponding estimated band gap energy of different-faceted CeO_2 and CN were determined to describe the proper band structures of $CeO_2/g-C_3N_4$ composites (Fig. S7a, b and Table S3). From the formula $(\alpha h\nu)n = k(h\nu\text{-}E_g)$, where α, $h\nu$, k and E_g referred to absorption coefficient, absorption energy, a constant relied on the effective masses, band gap energy, respectively; and the parameter n was a pure number related to the different electronic transitions (n = 2 or 1/2 for indirect-allowed or direct-allowed transitions, respectively) [56]. The energy band gaps were calculated, *i.e.* 2.98, 3.09, 3.00, and 2.90 eV for CeO_2 {110}, {100} and {111} and CN (Fig. S7b), respectively. From the equations:

$$E_{VB} = \chi - E_e + 1/2E_g$$

$$E_{CB} = E_{VB} - E_g$$

where χ was the absolute electronegativity of the semiconductor (the values were 5.57 eV and 4.74 eV for CeO_2 and $g-C_3N_4$, respectively), E_e was 4.5 eV for the free electron energy on the hydrogen scale and E_g was band gap energy [57,58], the values of the VB and CB positions of CeO_2 {110} {100} {111} and CN were calculated and shown in Table S3. Based on the above results, the proper band structures of rCN{110}, cCN{100} and oCN{111} composites were described in Fig. S7c.

Furthermore, the photoelectrochemical measurement was an efficient technology to evaluate the interfacial charge separation dynamics, and the photocurrent intensity was related to both of the separation of photo-generated electrons and the efficient electron transfer [59,60]. Herein, the transient photocurrent density of CN, rCN{110}, cCN{100}, and oCN{111} were determine to confirm the crystal-plane-dependent interfacial interaction on photo-generated electron transfer. As shown in Fig. S8, it could be found that when the light source switched on and off, the photocurrent abruptly increased and decreased, respectively. The photocurrent density of $CeO_2/g-C_3N_4$ composites was higher than that of bare $g-C_3N_4$, in the order of rCN{110} > cCN{100} > oCN {111}. The result could propose that there were more efficient separation and transfer of photo-generated electrons in rCN{110} photocatalyst than that in cCN{100} and oCN{111} samples from different interfacial interaction.

3.4. Photocatalytic H_2 evolution

The photocatalytic performances of H_2 production on $CeO_2/g-C_3N_4$ nanocomposites with different CeO_2 crystal planes were evaluated under visible-light irradiation ($\lambda \geq 420$ nm). The pure CeO_2 had poor activity of H_2 production, and the photocatalytic performances of CeO_2 rods {110}, cubes {100}, and octahedron {111} were in the order of {110} > {100} > {111}. From the photocatalytic activities (Fig. 4a), it could be seen that the $CeO_2/g-C_3N_4$ nanocomposites had better H_2 evolution as compared with pristine CeO_2 and CN. After irradiated 5 h, the rCN composite exhibited the superior H_2 production with 5500 μmol/g, cCN sample was followed, and oCN was the poorest. The obtained results suggested that the crystal-plane-dependent $CeO_2/g-C_3N_4$ interaction had efficient effects on the photocatalytic performance. The order of the H_2 evolution were: rCN{110} > cCN

{100} > oCN{111}, which was the same as the sequence of the interfacial electron-hole separation rates, and the amount of the oxygen defect and Ce^{3+}/Ce^{4+} ration. The photocatalytic stability was further confirmed and the recycling test of rCN was shown in Fig. 4b. In the four cycles, there was no obvious decreased H_2 production, suggesting that the obtained rCN exhibited superior photostability during reaction time.

3.5. Crystal-faceted $CeO_2/g-C_3N_4$ interaction

The photoelectrochemical, XPS, Raman, ESR results and photoctalytic performances suggested that the charge-separation efficiency, oxygen defects, Ce^{3+}/Ce^{4+} reversibility pairs and hydrogen evolution were greatly dependent on the crystal-faceted $CeO_2/g-C_3N_4$ interaction, in the order: rCN{110} > cCN{100} > oCN{111}. Therefore, the crystal-plane dependent interface was crucial, which was worthy to be explored in detail. Herein, FT-IR, XPS and DFT calculations were carried out to investigate the interfacial electronic interaction.

The FT-IR spectra of CN, rCN, cCN and oCN naocomposites were shown in Fig. 5a. The characteristic vibrational peaks attributed to $g-C_3N_4$ were observed on all samples. A sharp peak at 820 cm^{-1} was coming from the bending vibration of heptazine rings on $g-C_3N_4$, a series of peaks ranging from 1100 to 1800 cm^{-1} were ascribed to the typical stretching modes of heterocycles [61]. Furthermore, there was a board absorption peak at 3000-3500 cm^{-1} assigned to the stretching vibration of N−H bond associated with primary and secondary amino groups [61]. When we enlarged the region of 3600-2800 cm^{-1} (Fig. 5b), it was observed that the intensity ratio of I_{3100}/I_{3180} was increased *via* $g-C_3N_4$ coupled with CeO_2. Generally, the relative peak intensity in FT-IR was mainly attributed to the dipole moment, owing to the electronegativity, vibration models, *etc.* Based on the FT-IR spectra, it was proposed that the inter-electric field between $g-C_3N_4$ and CeO_2 was built, leading to the change of dipole moment of amino groups on $g-C_3N_4$. In order to further explore the interfacial interaction between different faceted CeO_2 and $g-C_3N_4$, XPS characterization was determined.

XPS was an efficient technology to elucidate the chemical states and electronic structures of the elements, and XPS spectra of C 1 s and N 1 s on CN, rCN, cCN and oCN samples were shown in Fig. 6a, b, respectively. According to literatures, in the C 1 s spectra (Fig. 6a), the peaks located at 287.8, 284.6 eV were assigned to the sp^2-bonded carbon atom (N−C = N) in aromatic rings of $g-C_3N_4$ and carbon contamination, respectively [62,63]. As for the N 1 s spectra in Fig. 6b, the broad peak was fitted into four peaks. The peaks centered at *ca.* 398.2 and 399.7 eV derived from the sp^2-hybridized nitrogen atom (C = N−C) and tertiary nitrogen (N–C_3 or H–N–C_2), respectively, and the other two peaks at *ca.* 400.8 and 404.0 eV were recognized as amino groups and charge effect localization in heterocycles, respectively [62,63]. Interesting, in comparison of CN, rCN, cCN and oCN samples, the binding energies of C 1 s and N 1 s peaks, ascribed to sp^2-bonded carbon and nitrogen atoms in s-triazine ring, shifted to lower values on rCN{110} nanocomposite. The phenomenon suggested that more electrons were donated to N, C 2p orbitals of s-triazine ring on the $g-C_3N_4$. On the basis of the coordination unsaturated Ce atom (Ce_{CUS}) on CeO_2 {110}, it was speculated that the C and N atoms with the strong electronegativity was inclined to withdraw the Ce 4f electron, and then the charge density on $g-C_3N_4$ was increased. On the other hand, for the cCN{100} sample, it was found that the binding energies ascribed to C and N were blue-shift compared to pure $g-C_3N_4$ (Fig. 6a, b). Considering of the coordination unsaturated O atom (O_{CUS}) on CeO_2 {100}, the electronegativity of O atom was stronger than C or N atoms, withdrawn the C and N electrons of $g-C_3N_4$, and thus the charge density on $g-C_3N_4$ was decreased. And Fig. 3a also confirmed that O atom obtained electrons from $g-C_3N_4$ on cCN, because the binding energy shifted to low value and then the charge density on O atom was increased. For oCN{111}, the binding energies shifted a little (Fig. 6a, b), might resulted from the stability of
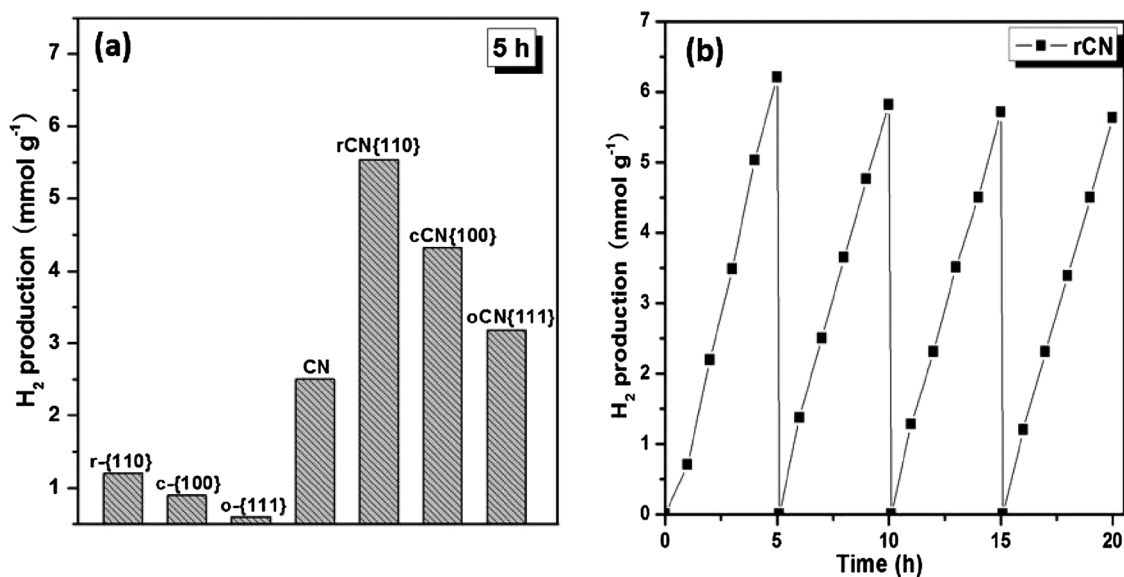
Fig. 4. (a) H$_2$ production of CeO$_2$ nanorods, cubes, octahedrons, CN, rCN, cCN, and oCN composites under visible light irradiation after 5 h; (b) the recycling rest of H$_2$ production of rCN.
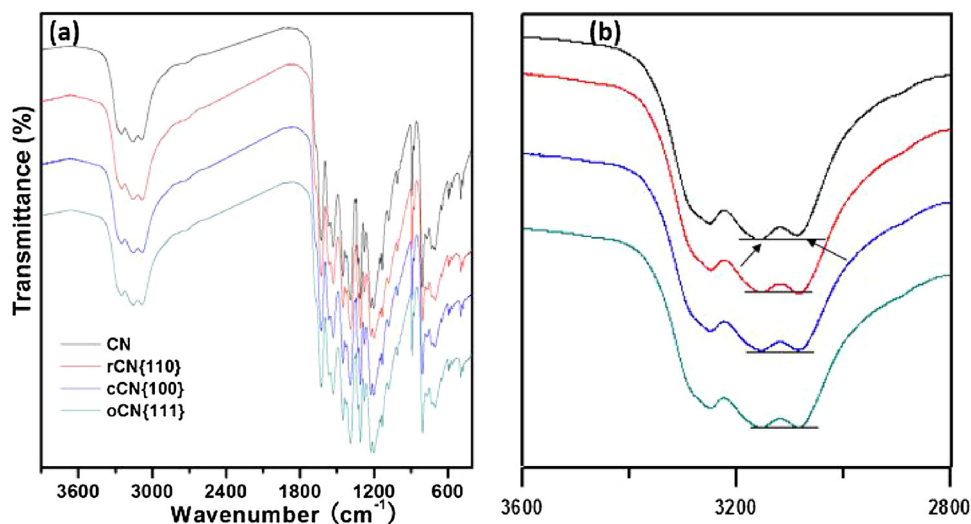

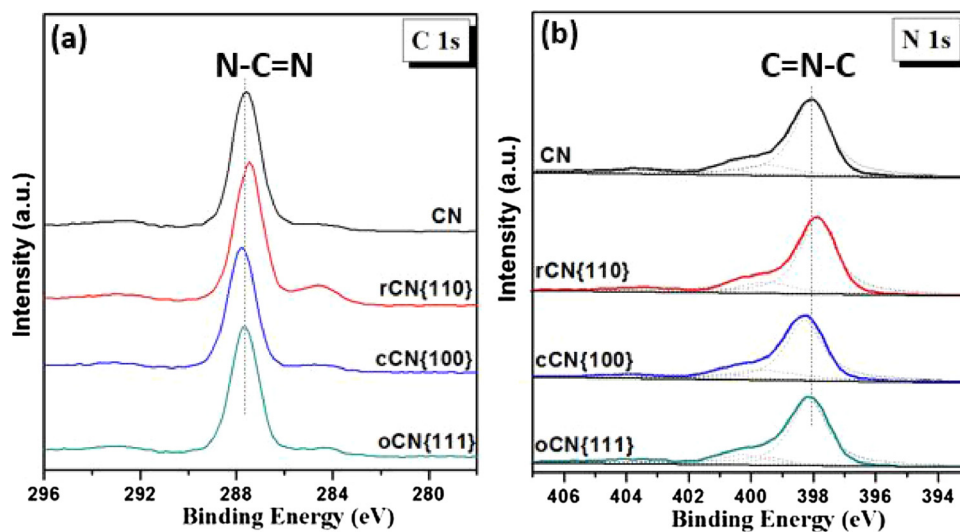**Fig. 5.** (a) FT-IR spectra of CN, rCN, cCN, and oCN composites; (b) the enlarged FT-IR spectra between 3600-2800 cm^{-1}.

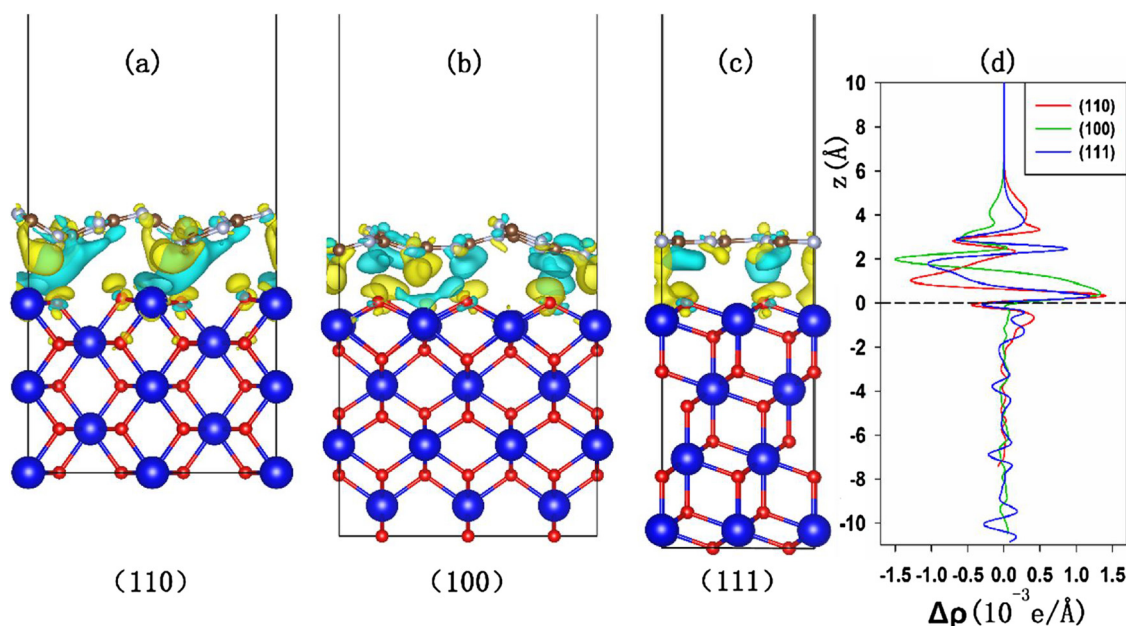**Fig. 6.** XPS spectra of (a) C 1 s; and (b) N 1 s of CN, rCN, cCN, and oCN.

Fig. 7. 3D Charge density differences for g-C$_3$N$_4$/CeO$_2$ composite with (a) (110); (b) (100); (c) (111) crystallographic planes. The blue and red balls represented Ce and O atom, and the yellow and cyan regions represented charge accumulation and depletion, respectively; the isosurface value was 0.005 e/Å^3. (d) Planar averaged charge density difference for the three different crystallographic planes as a function of position in the Z-direction of which the zero was referred to the uppermost surface layer (For interpretation of the references to colour in this figure legend, the reader is referred to the web version of this article.).

CeO$_2$ {111} surface.

In order to accurately describe and confirm the electron transfer process on the CeO$_2$/g-C$_3$N$_4$ interface, the charge density differences of rCN, cCN, and oCN were calculated and the corresponding result was shown in Fig. 7. The discrepancy of interactions in g-C$_3$N$_4$/CeO$_2$ can be visualized by three-dimensional charge density difference of $\Delta\rho = \rho_{g-C_3N_4/CeO_2} - \rho_{g-C_3N_4} - \rho_{CeO_2}$, where $\rho_{g-C_3N_4/CeO_2}$, $\rho_{g-C_3N_4}$ and ρ_{CeO_2} were the charge densities of the composite, g-C$_3$N$_4$ and CeO$_2$ surfaces in the same configuration, respectively. In comparison of rCN, cCN, and oCN, the plots shown that charge transfer occurred most significantly on the CeO$_2$ (110), whereas CeO$_2$ (100) taken second place. And the intensity of charge transfer process at the interface was in the order of rCN{110} > cCN{100} > oCN{111}. In schematic diagram, the cyan region indicated charge depletion, and the yellow region suggested charge accumulation. Based on that, for rCN{110} interface region, charge was increased in N and C atoms of g-C$_3$N$_4$, and reduced in Ce atoms of CeO$_2$ {110}; for cCN{100} interface region, charge was reduced in N and C atoms of g-C$_3$N$_4$, and increased in O atoms of CeO$_2$ {100}; for oCN{111} interface region, little charge change was observed. Combined with the XPS results, it was suggested that at rCN {110} interface, Ce 4f electron transferred to C and N atoms of g-C$_3$N$_4$; whereas, at cCN{100} interface, O atom withdrawn electrons from C and N atoms of g-C$_3$N$_4$; oCN{111} interface was stable and the charge transfer was negligible. Therefore, in rCN{110} composite, the photo-generated electrons would transfer to r-CeO$_2$ {110}; whereas, in cCN {100} composite, the photo-generated electrons would transfer to g-C$_3$N$_4$. The different direction of photo-generated electron transfer was attributed to the build-in electric field of CeO$_2$/g-C$_3$N$_4$, which acted as a driving force to the separation and transfer of the photo-generated electrons and then influenced the photocatalytic performance.

4. Conclusions

CeO$_2$/g-C$_3$N$_4$ composites were synthesized with tunable CeO$_2$ {110}, {100}, {111} crystal facets. It was found that the crystal-plane-dependent interactions at CeO$_2$/g-C$_3$N$_4$ interface were various, the photocatalytic H$_2$ evolution, separation of photo-generated hole and electron were in the order of rCN{110} > cCN{100} > oCN{111}. The

above difference was resulted from the built-in electric field at the interface of CeO$_2$/g-C$_3$N$_4$ composites. The rCN{110}composite had much stronger interaction at interface, leading to faster separation of electron-hole pairs, more Ce^{3+} species, and better photocatalytic activity.

Appendix A. Supplementary data

Supplementary material related to this article can be found, in the online version, at doi:https://doi.org/10.1016/j.apcatb.2018.07.022.

References

[1] S. Chu, A. Majumdar, Nature 488 (2012) 294–303.
[2] J. Liu, Y. Liu, N. Liu, Y. Han, X. Zhang, H. Huang, Y. Lifshitz, S.T. Lee, J. Zhong, Z. Kang, Science 347 (2015) 970–974.
[3] J. Luo, J.H. Im, M.T. Mayer, M. Schreier, M.K. Nazeeruddin, N.G. Park, S.D. Tilley, H.J. Fan, M. Grätzel, Science 345 (2014) 1593–1596.
[4] S. Mansingh, D.K. Padhi, K.M. Parida, Catal. Sci. Technol. 7 (2017) 2772–2781.
[5] Y.C. Zhang, Z. Li, L. Zhang, L. Pan, X.W. Zhang, L. Wang, F. Aleem, J.J. Zou, Appl. Catal. B Environ. 224 (2018) 101–108.
[6] X.J. Yao, Y. Xiong, W.X. Zou, L. Zhang, S.H. Wu, X. Dong, F. Gao, Y. Deng, C.J. Tang, Z. Chen, L. Dong, Y. Chen, Appl. Catal. B Environ. 144 (2014) 152–165.
[7] X. Wang, J.A. Rodriguez, J.C. Hanson, D. Gamarra, A. Martínez-Arias, M. Fernández-García, J. Phys. Chem. B 110 (2006) 428–434.
[8] P. Jasinski, T. Suzuki, H.U. Anderson, Sens. Actuators B Chem. 95 (2003) 73–77.
[9] X.H. Lu, T. Zhai, H.N. Cui, J.Y. Shi, S.L. Xie, Y.Y. Huang, C.L. Liang, Y.X. Tong, J. Mater. Chem. 21 (2011) 5569–5572.
[10] L.J. Xu, J.L. Wang, Environ. Sci. Technol. 46 (2012) 10145–10153.
[11] D. Jiang, W.Z. Wang, S.M. Sun, L. Zhang, Y.L. Zheng, ACS Catal. 5 (2015) 613–621.
[12] M.M. Khan, S.A. Ansari, D. Pradhan, D.H. Han, J. Lee, M.H. Cho, Ind. Eng. Chem. Res. 53 (2014) 9754–9763.
[13] S.L. Xie, Z.L. Wang, F.L. Cheng, P. Zhang, W.J. Mai, Y.X. Tong, Nano Energy 34 (2017) 313–337.
[14] J.B. Cai, X.Q. Wu, S.X. Li, F.Y. Zheng, Appl. Catal. B Environ. 201 (2017) 12–21.
[15] Y.G. Wang, F. Wang, Y.T. Chen, D.F. Zhang, B. Li, S.F. Kang, X. Li, L.F. Cui, Appl. Catal. B Environ. 147 (2014) 602–609.
[16] N. Zhang, X.Z. Fu, Y.J. Xu, J. Mater. Chem. 21 (2011) 8152–8158.
[17] M.H. Li, S.J. Zhang, L. Lv, M.S. Wang, W.M. Zhang, B.C. Pan, Chem. Eng. J. 229

(2013) 118–125.

[18] S. Kumar, A.K. Ojha, D. Patrice, B.S. Yadav, A. Materny, Phys. Chem. Chem. Phys. 18 (2016) 11157–11167.

[19] S. Ijaz, M.F. Ehsan, M.N. Ashiq, T. He, Catal. Sci. Technol. 5 (2015) 5208–5215.

[20] M.J. Muñoz-Batista, M. Fernández-García, A. Kubacka, Appl. Catal. B Environ. 164 (2015) 261–270.

[21] X. Chen, J. Zhang, X. Fu, M. Antonietti, X. Wang, J. Am. Chem. Soc. 131 (2009) 11658–11659.

[22] M.L. Li, L.X. Zhang, M.Y. Wu, Y.Y. Du, X.Q. Fan, M. Wang, L.L. Zhang, Q.L. Kong, J.L. Shin, Nano Energy 19 (2016) 145–155.

[23] M.J. Muñoz-Batista, M.A. Nasalevich, T.J. Savenije, F. Kapteijn, J. Gascon, A. Kubacka, M. Fernández-García, Appl. Catal. B Environ. 176–177 (2015) 687–698.

[24] X.J. She, H. Xu, H.F. Wang, J.X. Xia, Y.H. Song, J. Yan, Y.G. Xu, Q. Zhang, D.L. Du, H.M. Li, Dalton Trans. 44 (2015) 7021–7031.

[25] M. Nolan, S.C. Parker, G.W. Watson, Surf. Sci. 595 (2005) 223–232.

[26] P. Li, Y. Zhou, Z.Y. Zhao, Q.F. Xu, X.Y. Wang, M. Xiao, Z.G. Zou, J. Am. Chem. Soc. 137 (2015) 9547–9550.

[27] Z.L. Wu, A.K.P. Mann, M.J. Li, S.H. Overbury, J. Phys. Chem. C 119 (2015) 7340–7350.

[28] C.S. Pan, J. Xu, Y.J. Wang, D. Li, Y.F. Zhu, Adv. Funct. Mater. 22 (2012) 1518–1524.

[29] W.X. Zou, C.Y. Ge, M.Y. Lu, S.G. Wu, Y.Z. Wang, J.F. Sun, Y. Pu, C.J. Tang, F. Gao, L. Dong, RSC Adv. 5 (2015) 98335–98343.

[30] G. Kresse, J. Hafner, Phys. Rev. B 47 (1993) 558–561.

[31] G. Kresse, J. Furthmüller, Phys. Rev. B 54 (1996) 11169–11186.

[32] G. Kresse, J. Furthmüller, Comput. Mater. Sci. 6 (1996) 15–50.

[33] P.E. Blöchl, Phys. Rev. B 50 (1994) 17953–17979.

[34] J.P. Perdew, K. Burke, M. Ernzerhof, Phys. Rev. Lett. 77 (1996) 3865.

[35] S. Dudarev, G. Botton, S. Savrasov, C. Humphreys, A. Sutton, Phys. Rev. B 57 (1998) 1505–1509.

[36] Z. Yang, X. Yu, Z. Lu, S. Li, K. Hermansson, Phys. Lett. A 373 (2009) 2786–2792.

[37] H.J. Monkhorst, J.D. Pack, Phys. Rev. B Condens. Matter Mater. Phys. 13 (1976) 5188.

[38] E. Kümmerle, G. Heger, J. Solid State Chem. 147 (1999) 485–500.

[39] X. Wang, K. Maeda, A. Thomas, K. Takanabe, G. Xin, J.M. Carlsson, K. Domen, M. Antonietti, Nat. Mater. 8 (2009) 76–80.

[40] X.F. Yang, Z.P. Chen, J.S. Xu, H. Tang, K.M. Chen, Y. Jiang, ACS Appl. Mater. Interface 7 (2015) 15285–15293.

[41] F. Lei, Y. Sun, K. Liu, S. Gao, L. Liang, B. Pan, Y. Xie, J. Am. Chem. Soc. 136 (2014) 6826–6829.

[42] Z.F. Huang, J. Song, L. Pan, F. Lv, Q. Wang, J.J. Zou, X. Zhang, L. Wang, Chem.

[43] W.X. Zou, L. Zhang, L.C. Liu, X.B. Wang, J.F. Sun, S.G. Wu, Y. Deng, C.J. Tang, F. Gao, L. Dong, Appl. Catal. B Environ. 181 (2016) 495–503.

[44] X.J. Bai, L. Wang, R.L. Zong, Y.H. Lv, Y.Q. Sun, Y.F. Zhu, Langmuir 29 (2013) 3097–3105.

[45] S.X. Yu, Y.H. Zhang, F. Dong, M. Li, T.R. Zhang, H.W. Huang, Appl. Catal. B Environ. 226 (2018) 441–450.

[46] J. Liu, J. Ke, D.G. Li, H.Q. Sun, P. Liang, X.G. Duan, W.J. Tian, M.O. Tadé, S.M. Liu, S.B. Wang, ACS Appl. Mater. Interface 9 (2017) 11678–11688.

[47] P.V. Zinin, L.C. Ming, S.K. Sharma, V.N. Khabashesku, X. Liu, S. Hong, S. Endo, T. Acosta, Chem. Phys. Lett. 472 (2009) 69–73.

[48] I. Papailias, T. Giannakopoulou, N. Todorova, D. Demotikali, T. Vaimakis, C. Trapalis, Appl. Surf. Sci. 358 (2015) 278–286.

[49] J.Y. Qin, J.P. Huo, P.Y. Zhang, J. Zeng, T.T. Wang, H.Q. Zeng, Nanoscale 8 (2016) 2249–2259.

[50] S.J. Chang, M. Li, Q. Hua, L.J. Zhang, Y.S. Ma, B.J. Ye, W.X. Huang, J. Catal. 293 (2012) 195–204.

[51] M. Lohrenscheit, C. Hess, ChemCatChem 8 (2016) 523–526.

[52] M. Piumetti, S. Bensaid, N. Russo, D. Fino, Appl. Catal. B Environ. 165 (2015) 742–751.

[53] B.M. Reddy, P. Bharali, G. Thrimurthulu, P. Saikia, L. Katta, S.E. Park, Catal. Lett. 123 (2008) 327–333.

[54] K. Zhao, J. Qi, H.J. Yin, Z.M. Wang, S.L. Zhao, X. Ma, J.W. Wan, L. Chang, Y. Gao, R.B. Yu, Z.Y. Tang, J. Mater. Chem. A 3 (2015) 20465–20470.

[55] L. Qi, Q. Yu, Y. Dai, C.J. Tang, L.J. Liu, H.L. Zhang, F. Gao, L. Dong, Y. Chen, Appl. Catal. B Environ. 119–120 (2012) 308–320.

[56] H.W. Huang, Y. He, Z.S. Lin, L. Kang, Y.H. Zhang, J. Phys. Chem. C 117 (2013) 22986–22994.

[57] Z.M. Yang, G.F. Huang, W.Q. Huang, J.M. Wei, X.G. Yan, Y.Y. Liu, C. Jiao, Z. Wan, A.L. Pan, J. Mater. Sci. A 2 (2014) 1750–1756.

[58] Y. Yuan, G.F. Huang, W.Y. Hu, D.N. Xiong, B.X. Zhou, S.L. Chang, W.Q. Huang, J. Phys. Chem. Solids 106 (2017) 1–9.

[59] F. Wang, X.X. He, L.M. Sun, J.Q. Chen, X.J. Wang, J.J. Xu, X.G. Han, J. Mater. Chem. A 6 (2018) 2091–2099.

[60] S. Patnaik, G. Swain, K.M. Parida, Nanoscale 10 (2018) 5950–5964.

[61] S.Z. Hu, L. Ma, J.G. You, F.Y. Li, Z.P. Fan, G. Lu, D. Liu, J.Z. Gui, Appl. Surf. Sci. 311 (2014) 164–171.

[62] D. Gao, Q. Xu, J. Zhang, Z. Yang, M. Si, Z. Yan, D. Xue, Nanoscale 6 (2014) 2577–2581.

[63] N. Tian, H.W. Huang, C.Y. Liu, F. Dong, T.R. Zhang, X. Du, S.X. Yu, Y.H. Zhang, J. Mater. Chem. A 3 (2015) 17120–17129.